Diastereomeric Configuration Drives an On-Surface Specific Rearrangement into Low Bandgap Non-Benzenoid Graphene Nanoribbons.

Federico Villalobos,[1,2‡] Jesús I. Mendieta-Moreno,[2‡] Jorge Lobo-Checa,[3,4] Sara P. Morcillo,[1] José I. Martínez,[2] José María Gómez-Fernández,[2] Pedro L. de Andres,[2] José A. Martin-Gago,[2] Juan M. Cuerva,[1] Araceli G. Campaña,[1*] Carlos Sánchez-Sánchez[2*].

1 Departamento de Química Orgánica, Universidad de Granada (UGR), Unidad de Excelencia de Química UEQ, C. U. Fuentenueva, 18071 Granada, Spain.

2 ESISNA Group, Instituto de Ciencia de Materiales de Madrid (ICMM-CSIC), Sor Juana Inés de la Cruz 3, 28049 Madrid, Spain.

3 Instituto de Nanociencia y Materiales de Aragón (INMA), CSIC−Universidad de Zaragoza, Zaragoza 50009, Spain.

4 Departamento de Física de la Materia Condensada, Universidad de Zaragoza, Zaragoza 50009, Spain.

KEYWORDS

Stereochemistry, Configuration, On-Surface Synthesis, Non-Benzenoid Rings, Chevron-like GNR, Bandgap Engineering, Au Adatom, Quantum-Mechanical Calculations, Scanning Probe Microscopy.

ABSTRACT

Stereochemistry, usually associated to the three-dimensional arrangement of atoms in molecules, is crucial in processes like life functions, drug action, or molecular reactions. This three-dimensionality typically originates from sp^3 hybridization in organic molecules, but it is also present in out-of-plane sp^2-based molecules as a consequence of helical structures, twisting processes, and/or the presence of non-benzenoid rings, the latter significantly influencing their global stereochemistry and leading to the emergence of new exotic properties. In this sense, on-surface synthesis methodologies provide the perfect framework for the precise synthesis and characterization of organic systems at the atomic scale, allowing for the accurate assessment of the associated stereochemical effects. In this work, we demonstrate the importance of the initial diastereomeric configuration in the surface-induced skeletal rearrangement of a substituted cyclooctatetraene (COT) moiety–a historical landmark in the

understanding of aromaticity–into a cyclopenta[c,d]azulene (CPA) one in a chevron-like graphene nanoribbon (GNR). These findings are evidenced by combining bond-resolved scanning tunneling microscopy with theoretical ab-initio calculations. Interestingly, the major well-defined product, a CPA chevron-like GNR, exhibits the lowest bandgap reported to date for an all-carbon chevron-like GNR, as evidenced by scanning tunneling spectroscopy measurements. This work paves the way for the rational application of stereochemistry in the on-surface synthesis of novel graphene-based nanostructures.

INTRODUCTION

Understanding molecular spatial arrangements is essential to properly describing their properties.[1] Stereochemistry is devoted to this topic, considering both static (configuration) and dynamic (conformation) temperature-depending situations. Stereochemistry is at the core of various disciplines, from chemistry to biology, as it is essential for correctly describing chemical reactions.[2] Although the more common three-dimensional situations in organic chemistry are related to molecules composed of sp^3-hybridized carbon atoms, it is also relevant in out-of-plane geometries composed of olefins and conjugated compounds, typically considered as planar entities. Among the latter, graphene-based nanostructures like nanographenes (NG)[3,4] and graphene nanoribbons (GNRs)[5] might be of particular interest given their unique properties. In fact, the stereochemistry of graphene-based nanomaterials is a flourishing field, as different strategies have been developed to introduce curvature (i.e. three-dimensionality) in them. For example, curvature has been achieved by steric interactions between rings or substituents in close proximity, which induce a helical twist in polyaromatic systems, as is the case for twistacenes[6] or helicenes;[7–9] or by the addition of structural strain through the incorporation of non-benzenoid rings in distorted NG.[10,11] This distortion also affects their functionalities, enabling new properties like enhanced solubility, tuned optoelectronic properties,[12] improved non-linear optics like two-photon absorption,[13] or chiroptical properties.[14] Among the strategies mentioned above to induce curvature, the incorporation of non-benzenoid rings might also influence the aromaticity of the nanostructures, which is another important attribute that can modify the optoelectronic properties,[15] introduce magnetism,[16] or enhance the charge carrier mobility.[17]

In this regard, cyclooctatetraene (COT, Figure 1) has been a historical landmark in chemistry since its first preparation, being crucial for understanding the concept of aromaticity.[18] Despite being essentially antiaromatic, it develops a Jahn-Teller distortion that drives it out of planarity, resulting in a stable D_{2d} tub-shape cyclic tetraene. Surprisingly, the three-dimensional architecture of the COT unit presents a high interconversion barrier between the two degenerated D_{2d} tub-shape geometries, which is highly dependent on the degree and nature of the substituents, increasing the barrier by a benzoannulation process.[19–21] Therefore, configurationally stable structures at high temperatures can be obtained by the fusion of at least three benzenic subunits. For example, the calculated barrier for tribenzoannulated COT (triCOT) is ~ 1.91 eV.[19] Planar geometries present some degree of antiaromaticity and are considered intermediates during the interconversion between tub-shape geometries. However, theoretical work suggest that the interaction with a surface can avoid such intrinsic instability.[22,23] In this sense, the D_{2d} tub-shape stable configuration of the COT moiety constitutes an intriguing option for integrating curvature into GNRs, allowing the exploration of new functionalities and reactivities.[24,25]

The synthesis of extended graphene-based nanostructures such as GNRs remains challenging for in-solution chemistry due to their limited solubility and difficult full characterization. In this regard, the advent of on-surface synthesis (OSS) has been a breakthrough in the synthesis of novel graphene-

based nanoarchitectures, providing a powerful alternative to conventional synthesis in solution. The ability to perform experiments in ultra-high vacuum (UHV) conditions and at cryogenic temperatures allows for the synthesis and study of highly unstable and insoluble compounds unachievable by conventional bench chemistry.[26] The use of atomically sensitive microscopes, such as scanning tunneling microscopy (STM) and atomic force microscopy (AFM), enables single-molecule characterization[27,28] and manipulation. The dimensional restriction of the surface, moving from 3D in-solution chemistry to 2D OSS, has opened up a new range of unprecedented synthetic routes, and it has unlocked new reaction pathways, due to the catalytic properties of such surfaces.

Therefore, the combination of stable 3D configurations and 2D surfaces may lead to potential diastereomeric entities, which may translate into a specific type of reactions[29–32] that can be even more pronounced on chiral surfaces.[33–35] It is worth noting that the stereochemical outcome of reactions involving stereoisomers on surfaces has been largely overlooked.[36] As it has been demonstrated, surfaces tend to induce the planarization of distorted graphene-based nanostructures, even at the cost of severe skeletal rearrangements as is the case of benzoannulated tropone moieties.[37] Therefore, a similar behaviour can be expected for other benzoannulated high-membered rings like COT derivatives. However, the reaction pathway and the final product may differ depending on the starting stereochemistry.

In this work, we demonstrate the importance of the initial diastereomeric configuration in the specific skeletal rearrangement of a triCOT. Specifically, we show that the configurational stability of triCOT moieties, when incorporated into chevron-GNR precursors, allows the formation of stable concave and convex configurations that become diastereomeric geometries when adsorbed on a planar (gold) surface (Figure 1). These diastereomeric polymeric configurations govern the system's chemistry during the cyclodehydrogenation step, resulting in the planarization of the final GNR. Interestingly, only one of the diastereoisomers generates unprecedented non-benzenoid cyclopenta[c,d]azulene (CPA) moieties, yielding the lowest bandgap (1.43 eV) for an all-carbon-based chevron-like GNR. This work paves the way toward using stereochemistry in the rational on-surface synthesis of novel graphene-based nanostructures as it may open new reactions pathways.

RESULTS AND DISCUSSION

Figure 1 presents the dibrominated triCOT-type monomer (**Mono**) designed to yield novel chevron-GNRs on a surface upon sequential Ullmann-type and oxidative cyclodehydrogenation reactions. The well-defined in-solution distorted geometry of the monomer induced by the presence of the triCOT moiety, consistent with the high interconversion barriers between the equivalent configurations, results in two diastereomers when adsorbed on a surface due to the broken symmetry induced by it: concave (**Mono-Cc**) or convex (**Mono-Cx**) (see Figure 2b and 2f for the **Mono-Cc** and **Mono-Cx** 3D DFT optimized configurations, respectively). As a consequence, three different molecular self-assemblies appear upon room temperature (RT) deposition onto a Au(111) surface: (i) elongated irregular chains with a bright backbone (see red circle in Figure S1a), (ii) square-shaped linear aggregates (white circle in Figure S1a,b), and (iii) rhomboidal-shaped clusters that arrange into chains or trimers (Figure S1b blue and green circles, respectively). It is important to note that, according to our quantum ab-initio and molecular mechanical (QM/MM) simulations, the convex and concave configurations in the monomeric phase do not interconvert at RT, as the energy barrier for this process is relatively high

(1.59 eV, see Figure S2). The steric repulsion between neighboring hydrogen atoms from the benzene rings attached to the central ring and those from the benzene rings attached to the COT moiety hinders this interconversion (see red crosses in Figure S2a), as it had been suggested previously.[19–21]

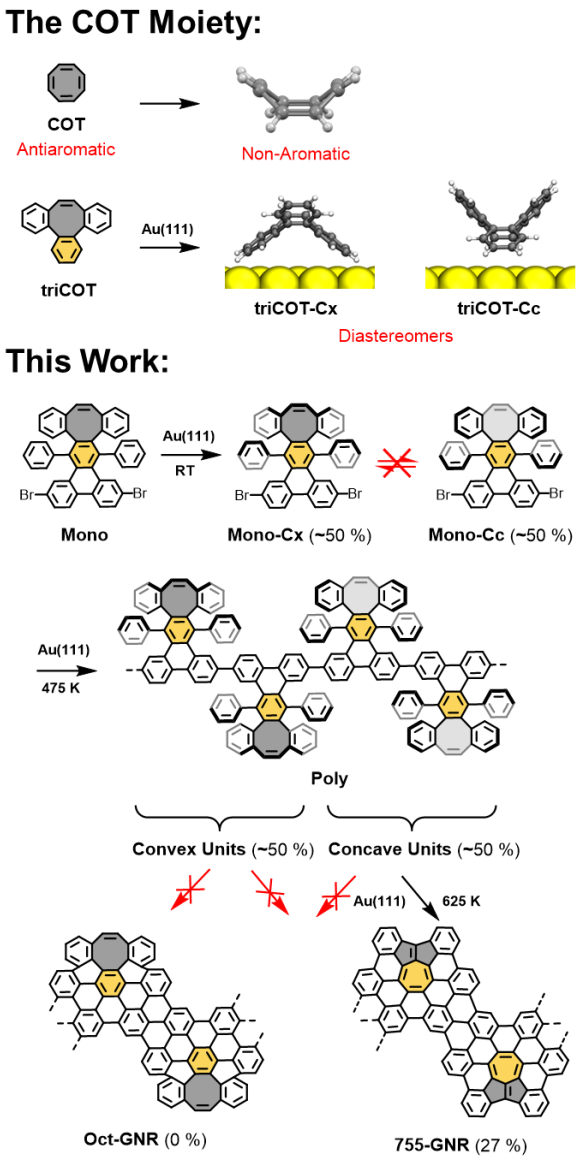

Figure 1. Top: Schematic representations of the 3D geometries of the gas-phase cyclooctatetraene (COT) and the on-surface tribenzoannulated COT (triCOT) moieties with its two possible on-surface configurations (convex and concave). Bottom: Schematic representation of the on-surface synthesis of the cyclopentaazulene-containing GNR **755-GNR**.

Interestingly, our high-resolution STM images allow us to unambiguously discern between both diastereomers, as the **Mono-Cc** is characterized by a double bright maximum at the outer narrower side (blue arrows in Figure 2c). At the same time, **Mono-Cx** exhibits a single bright feature at the center (green arrow in Figure 2g) due to the out-of-plane highest structural feature in each case. The STM simulations in Figure 2d,h clearly corroborate this assumption. Considering these aspects, we assign the elongated irregular chains to an alternating self-assembly of **Mono-Cc** stabilized by the π-π stacking between neighboring dibenzo[a,e]cyclooctene moieties (Figure S1c). On the other hand, the square-shaped aggregates correspond to the self-assembly of four **Mono-Cx** molecules rotated by approximately 90º relative to each other in a chiral configuration (Figure S1d). Finally, the rhomboidal-

shaped clusters are ascribed to the agglomeration of three tetramers, each composed of two **Mono-Cc** and two **Mono-Cx** arranged alternatingly, as depicted in Figure S1e.

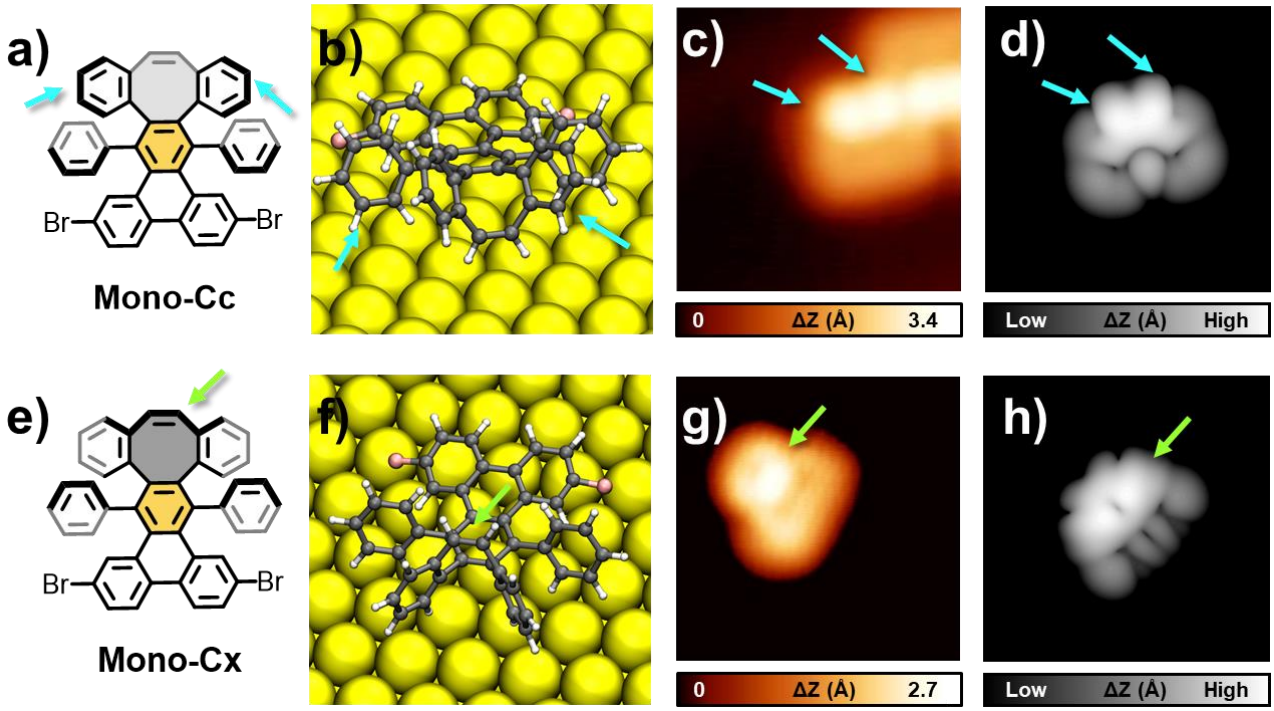

Figure 2. On-surface characterization of **Mono-Cc** and **Mono-Cx** on Au(111) at RT. **a)** Chemical model of **Mono-Cc**. Blue arrows depict the brightest features in the STM image c). **b)** QM/MM minimized structure of **Mono-Cc** on Au(111). **c)** Constant-current STM image of **Mono-Cc**. **d)** Simulated constant-current STM image of **Mono-Cc**. **e)** Chemical model of **Mono-Cx**. The green arrow depicts the brightest feature in the STM image g). **f)** QM/MM minimized structure of **Mono-Cx** on Au(111). **g)** Constant-current STM image of **Mono-Cx**. **h)** Simulated-constant current STM image of **Mono-Cx**. Scanning parameters were as follows: (**c**) 3.78 nm × 3.78 nm, 50 pA, − 0.05 V, (**g**) 3.78 nm × 3.78 nm, 10 pA, − 0.01 V.

Figure 3a shows an overview STM image of the Au(111) surface upon annealing at 475 K, which results in the formation of islands composed of molecular chains due to the Ullmann-like coupling between monomers. Interestingly, we identify two distinct types of interpolymeric interdigitation: a denser phase (red circle)[38] and a less densely-packed phase (white circle).[39] A detailed analysis of various high-resolution STM images, like the one presented in Figure 3b, sheds light on different interesting aspects. Firstly, the periodicity along the chains corresponds to 1.67 nm, which is in agreement with the theoretical value (1.76 nm) and with those reported for other chevron-like GNRs.[38] Secondly, the internal appearance observed in the monomeric phase at RT is preserved in the polymeric phase, allowing us to unambiguously assign them to the corresponding concave/convex configuration (see simulated images in Figure 3c). From these observations, two important conclusions can be extracted: (i) our correlation analysis indicates that there is a low correlation (0.218 ± 0.02 for first neighbors and 0.268 ± 0.001 for second neighbors, along the polymers) in the growth of the polymer, i.e. the growth is almost not influenced by the monomeric configuration, not very surprising considering the relatively large distance between adjacent monomers (around 1.80 nm); (ii) a statistical analysis on the number of concave/convex monomers in the monomeric and polymeric phases corroborates that the interconversion barrier in both cases is high enough to avoid a configuration change even at 475 K, with approximately 50 % of the monomers in each configuration (see Figure S3). In fact, the interconversion barrier at the polymeric phase is even larger (2.81 eV, see Figure S4) compared to the monomeric phase (1.59 eV). The presence of both diastereoisomers along the polymer

with low selectivity and their relative abundance will play a critical role in the atomic structure of the final GNRs, as shown below.

The system was then annealed to 625 K to complete the formation of the GNRs through a surface-assisted cyclodehydrogenation (CDH) reaction. Figure 3d shows the resulting GNRs, whose irregular appearance can be easily distinguished. This irregularity already indicates a lack of selectivity in the final shape of the GNR and, consequently, suggests the occurrence of intramolecular transformations. To determine the atomic structure of the final GNRs, bond-resolved STM (BR-STM) imaging with CO tips has been carried out. Figure S5 presents two different GNR segments where the main precursor compositions can be easily identified. Apart from the defective products resulting from the partial decomposition of the precursors during the CDH reaction (**Def-GNR**), up to three well-defined products are obtained: (i) cyclopenta[c,d]azulene-based GNRs (**755-GNR**), (ii) fully-hexagonal extended pristine chevron GNRs (**Ext-GNR**), (both being constitutional isomers of **Oct-GNR**), and (iii) the pristine chevron GNRs (**Prist-GNR**), which implies the loss of two carbon atoms (see Figure S6).

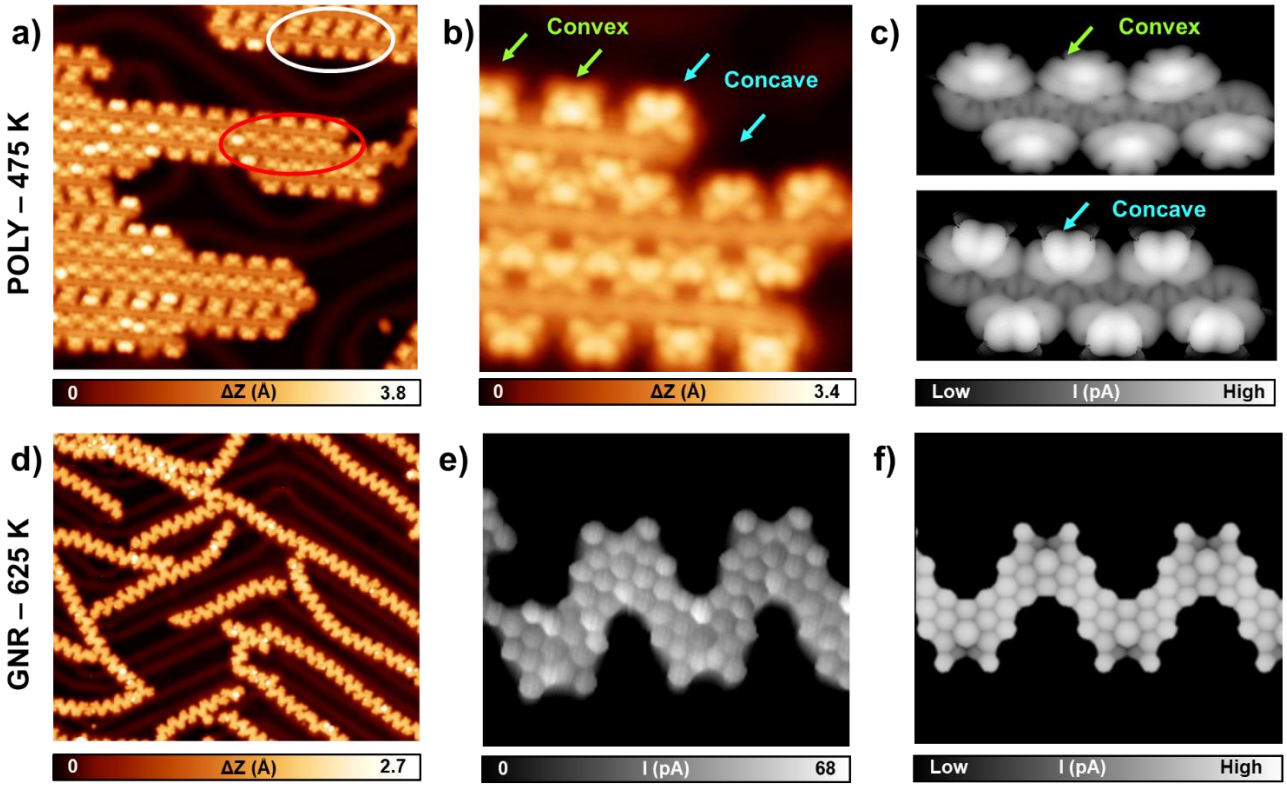

Figure 3. On-surface synthesis of **Poly** (475 K) and **755-GNR** (625 K) on a Au(111) surface. **a)** Topographic constant-current STM image of **Poly**. White and red circles depict the two types of interdigitations observed between polymers. **b)** Detailed constant-current STM image of **Poly**. Green/blue arrows depict convex/concave units. **c)** Simulations of the constant-current STM images of a six-unit oligomer of **Poly** with convex units (top) and concave units (bottom). **d)** Topographic constant-current STM image after annealing the Au(111) sample at 625 K. **e)** Constant-height bond-resolved STM image of a **755-GNR** segment. **f)** Simulation of a constant-height STM image of a **755-GNR** segment. Scanning parameters were as follows: (**a**) 27 nm × 27 nm, 100 pA, − 0.5 V, (**b**) 7.78 nm × 7.78 nm, 0.16 nA, − 0.05 V, (**d**) 54 nm × 45.25 nm, 20 pA, − 0.03 V, (**e**) 4.64 nm x 4.21 nm, 5.2 mV.

Interestingly, the first main conclusion is that there is no evidence for the formation of **Oct-GNR**, i.e. the curved triCOT moiety does not survive the CDH process but transforms into different planar moieties. This result is equivalent to the one observed for tribenzo-tropone moieties[40] and suggests the

low stability of high-membered rings at temperatures above 475 K on weakly interacting Au(111) surfaces. This instability can be understood by considering the elevated energy cost and accumulated stress associated with embedding the distorted configuration of the curved COT fully into the hexagonal graphene-like structure, preferring to reconstruct it into a planar configuration.

Regarding the products, a statistical analysis over approximately one thousand monomers indicates that the majority correspond to the **755-GNR**, accounting for 27% (see Figure S7), followed by 14% of the **Ext-GNR**. Interestingly, **755-GNR** constitutes a novel motif in GNRs, particularly rare in graphene-based nanostructures. Typically, seven-membered rings in graphene-like structures appear together with a single pentagonal ring, forming an azulene moiety.[16,41–49] Furthermore, to the best of our knowledge, this is the first report of an extended architecture bearing 755 moieties on surfaces where a pentalene and a heptagonal ring are interfused. Figure 3e,f shows the BR-STM and the simulated BR-STM images of a GNR segment where four consecutive cyclopenta[c,d]azulene-containing monomers are achieved.

Computational calculations were conducted to determine the reaction pathway from **Poly** to **755-GNR**, i.e. from the polymeric phase containing the **COT** units in convex and concave configurations to the **755-GNR** majority product. QM/ MM simulations[50] were employed to compute the activation barriers (free energy) for various reaction steps. It is worth noting that all our calculations have been carried out including a surface adatom, recurrently resulting in lower activation barriers (see Figures S8, S9, and S13 for a comparison of the activation barrier with and without adatom). Such an assumption is now well established in the field, with several results highlighting their critical role in surface-assisted reactions.[51–53]

Figure 4a, c displays the schematic representations of the partially cyclodehydrogenated **Semi-Cx** and **Semi-Cc** structures used as the starting point for our computational study. The choice of these structures has a two-fold motivation: (i) the experimental observation of the unusual skeletal rearrangement from triCOT to cyclopenta[c,d]azulene after the Ullmann coupling, i.e. during the cyclodehydrogenation step and (ii) the substantially higher activation barriers obtained when starting directly from the polymeric phase **Poly** without any prior partial CDH (see Figures S8, S10, S11). Additionally, Clair et al. recently observed a homologous semicyclodehydrogenated structure as a key intermediate in the cyclodehydrogenation process of the pristine chevron-like GNR on Au(111).[39] For clarity, the scheme in Figure 4a includes the labelling of the eight carbon atoms of the COT unit involved in the reaction pathway.

Based on our experimental findings on the decomposition of the octagonal ring, the first step must involve the rupture of this ring. In principle, this could occur by breaking one of the eight bonds in the COT unit. However, our theoretical results indicate that the energy barriers are not equal for all the bonds. It is especially relevant the mechanism critical dependence on the initial diastereomeric configuration (i.e. its concavity or convexity). Furthermore, as demonstrated below, only the concave configuration can yield the formation of **755-GNR**, thus being a specific reaction pathway. Among the eight bonds and the two possible diastereomeric configurations, the cleavage of the concave C_1-C_2 bond in the partially CDH intermediate via the insertion of the Au adatom presents the lowest activation barrier, 1.52 eV vs 4.39 eV for the convex configuration (see Figure S8 for the whole set of activation barriers). Such a difference in the activation energy can be ascribed to the curvature of each configuration, which makes the C_1-C_2 bond height relative to the surface to be 3.1 Å in **Semi-Cc** and 6.4 Å in **Semi-Cx** (note that the Au adatom is 2.3 Å above the surface). Such a structural constraint

makes the C_1-C_2 bond inaccessible to the adatom in the convex configuration (see Figure S12, S13 for further details on the transition states). Additionally, this step will constitute the rate-limiting step of the whole reaction, as shown below (see Figure S14 for the complete reaction pathway).

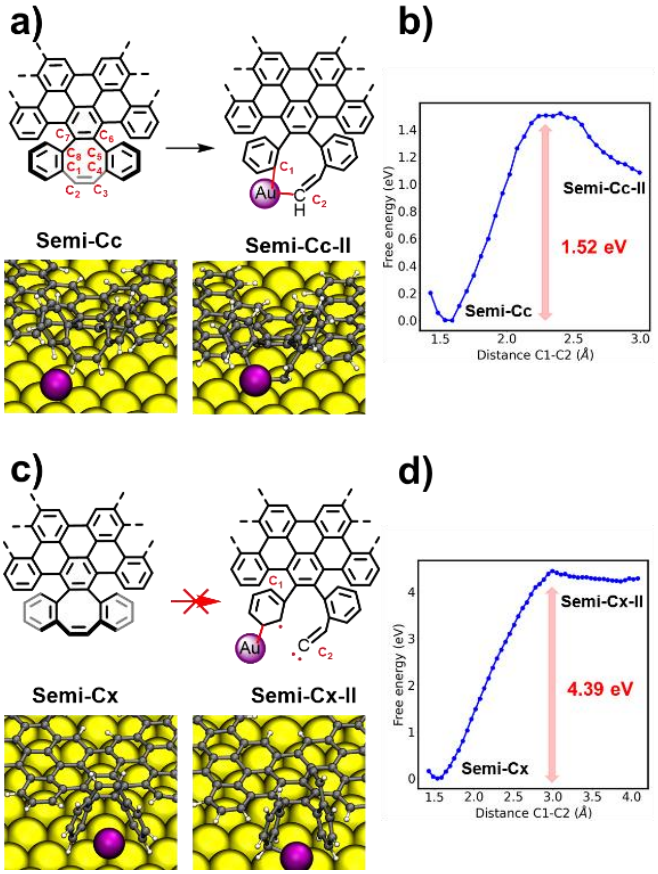

Figure 4. QM/MM calculated activation energies for the first reaction step (C1-C2 bond cleavage) of the COT-755 rearrangement, which shows the specificity of the process. **a)** Chemical sketch (top) and 3D models extracted from the QM/MM simulations (bottom) regarding **Semi-Cc**. **b)** Free energy diagram corresponding to a). **c)** Chemical sketch (top) and 3D models extracted from QM/MM simulations (bottom) regarding **Semi-Cx**. **d)** Free energy diagram corresponding to c).

Figure 5 displays the subsequent steps of the rearrangement pathway from **Semi-Cc** to the final product **Semi-Cc-VII**. For clarity, the chemical structures have been shortened in the figure for, focusing on those rings involved in the rearrangement. At step 2 (see Figure S15 for details of the transition state, TS), a gold-mediated homolytic aromatic addition happens from **C_2** to **C_6** after the homolytic breakage of the **C_2**-Au adatom bond. Intermediate **Semi-Cc-III,** based on a spiro compound with an unpaired electron in **C_7**, is formed after overcoming a 0.56 eV activation barrier. A gain of -3.04 eV in free energy takes place in step 3 after some rearrangements from the spiro **Semi-Cc-III** to the azulene intermediate **Semi-Cc-V**. First, a bond between **C_2** and **C_7** is formed from **Semi-Cc-III** to **Semi-Cc-IV**, creating the cyclopropane intermediate **Semi-Cc-IV.** Simultaneously, the radical formed in **C_3** bonds to the Au adatom (Figure S16). Second, from **Semi-Cc-IV** to **Semi-Cc-V,** the loss of a hydrogen atom at **C_2** and the homolytic breakage between **C_3** and the Au adatom enable the formation of the double bond between **C_2** and **C_3** in the transition state **Semi-Cc-IV-TS**. Subsequently, due to the norcaradiene–cycloheptatriene equilibrium,[54] the intermediate **Semi-Cc-IV-TS** shifts into the azulene intermediate **Semi-Cc-V** (total activation barrier: 0.64 eV). Lastly, a cyclodehydrogenation reaction

occurs in step 4 from **Semi-Cc-V** to **Semi-Cc-VII** (see Figure S17). After the cleavage of the bond between the Au adatom and C_1, a bond between C_3 and C_1 is formed, generating an unpaired electron at C_2 in **Semi-Cc-VI** (activation barrier: 0.31 eV). The loss of a hydrogen atom in C_1 mediated by the Au adatom and the formation of a double bond between C_3 and C_2 generate the 755-containing intermediate **Semi-Cc-VII** (activation barrier: 1.21 eV). Two further cyclodehydrogenations between adjacent phenyl rings from **Semi-Cc-VII** trigger the synthesis of the final **755-GNR**.

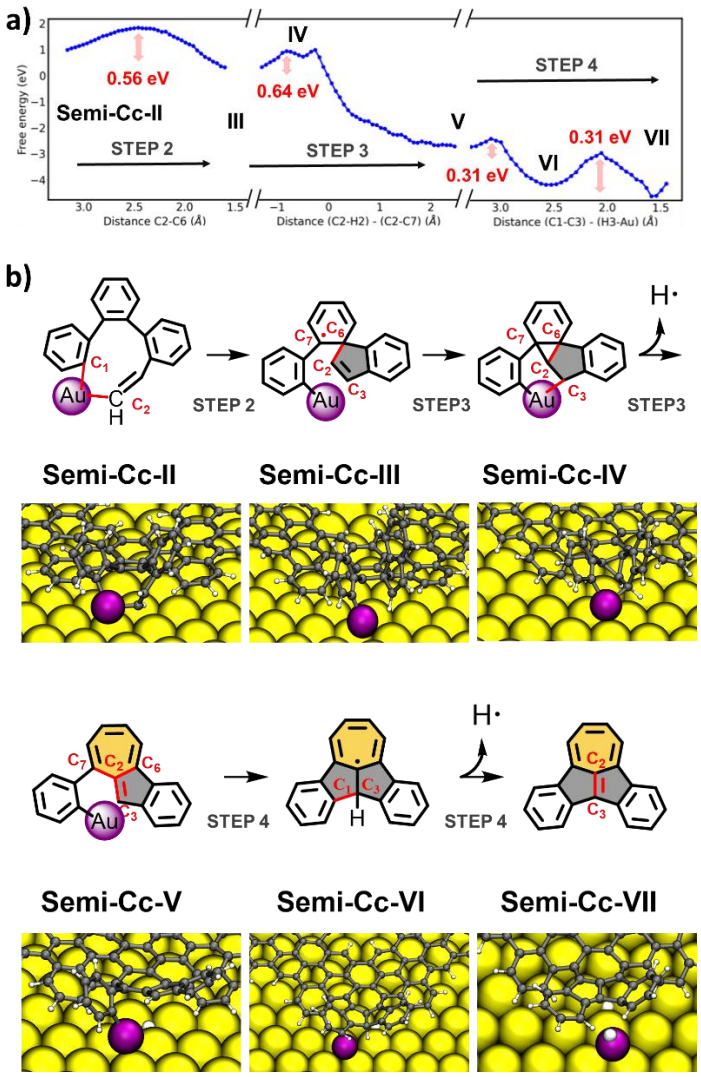

Figure 5. QM/MM simulations for steps 2, 3 and 4 of the rearrangement reactions from **Semi-Cc-II** to **Semi-Cc-VII**. **a)** Free energy diagram. Activation barriers are depicted in red. **b)** Chemical sketches and 3D models extracted from QM/MM simulation. Chemical sketches are shortened for clarity.

Once the synthesis of **755-GNR** and the rearrangement mechanism have been assessed, its local electronic structure on Au(111) was characterized by STS using a CO-functionalized tip. The red curve in Figure 6a represents a typical differential conductance (dI/dV) point spectrum recorded at the edge of the bay of the **755-GNR** (see red spot in the inset STM image of Figure 6a), showing peaks at – 1.38 eV, – 0.66 eV, 0.77 eV and 1.22 eV, all of them relative to the Fermi energy (V = 0 V). The **755-GNR** valence band (VB) has been assigned to the – 0.66 eV peak, and the peak at 0.77 eV has been identified as its conduction band (CB), resulting in the shortest bandgap for a purely carbon chevron GNR reported to date (1.43 eV).[38,55–58] This value is further confirmed by the dI/dV maps recorded at

these positions (see panels b-d), where the VB, CB and CB+1 can be discerned. It is worth mentioning that, while the states at – 0.66 eV and 1.22 eV can also be found in other non-755 ribbon segments, the state at 0.77 eV is characteristic of the 755 moieties. The 0.77 eV state can only be experimentally resolved in those 755 units fully embedded into other 755 units along the GNR (see Figure S18 for dI/dV maps in a longer segment including non-755 units). Panels e-g show the corresponding simulated dI/dV maps for an infinite **755-GNR** on the Au(111) surface, which are in qualitative good agreement with the experiment.

In this respect, it is interesting to note that, according to our computed band diagrams (Figure S19) corresponding to the three different products obtained (**755-GNR**, **Ext-GNR**, and **Prist-GNR**), new bands emerge in the **755-GNR**, which are responsible for the bandgap shortening in comparison to other all-carbon GNRs. These results show that including a cyclopentaazulene unit embedded in a GNR leads to a deep modification of its electronic properties.

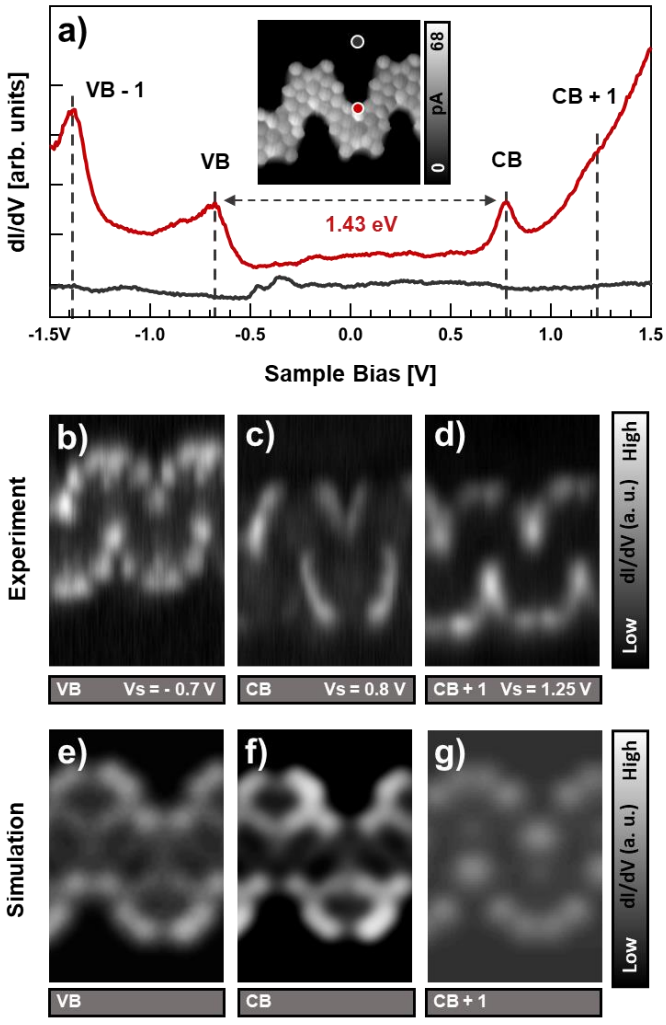

Figure 6. Electronic characterization of a **755-GNR** segment. **a)** STS point spectra obtained with a CO-tip. The acquisition position of the spectra is color coded at the BR-STM image. For the determination of the bandgap, the maxima of the VB and the CB have been considered, as indicated by dashed lines. **b)** to **d)** Constant-height dI/dV maps at different bias values. **e)** to **g)** Simulated dI/dV maps from the gas-phase orbitals of an infinite **755-GNR**. Scanning parameters were as follows: (**a**) BR-STM image: 3.24 nm × 3.24 nm, 5.2 mV. Point spectra: V_{Mod} = 20 mV; (**b**) 3.24 nm × 4.67 nm, V_{Mod} = 20 mV; (**c**) 3.24 nm × 4.67 nm, V_{Mod} = 20 mV (**d**) 3.24 nm × 4.67 nm, V_{Mod} = 20 mV.

CONCLUSIONS

Using STM and computational calculations, we have demonstrated the significance of the initial diastereomeric configuration in the surface-assisted specific skeletal rearrangement of a triCOT moiety. Specifically, we have shown that only the concave polymeric configuration of the triCOT transforms into a cyclopenta[c,d]azulene moiety when incorporated into a chevron-like graphene nanoribbon. QM/MM calculations confirm that the whole rearrangement process is mediated by a surface Au adatom in a specific manner. Additionally, we have studied the electronic properties of the unprecedented **755-GNR** with STS spectroscopy and dI/dV mapping, which reveals a bandgap narrowing due to the presence of the non-benzenoid cyclopenta[c,d]azulene moiety and resulting in the shortest bandgap for a fully-carbon chevron-like GNR reported to date. This work contributes to a deeper understanding of the stability of higher-order non-benzenoid rings and the impact of their configuration on on-surface reactions, paving the way for the rational tailoring of the properties of GNRs, such as the electronic bandgap, through the stereochemistry of non-benzenoid rings.

ASSOCIATED CONTENT

Materials and methods; the room temperature phase; monomeric interconversion barrier; statistical analysis; polymeric interconversion barrier; composition of the GNRs; Statistical analysis of the outcomes of the cyclodehydrogenation reaction; summary of the computed activation energies; selected reaction steps; complete reaction pathway; extended dI/dV maps; computed band diagrams; in-solution synthesis; NMR spectra.

AUTHOR INFORMATION

CORRESPONDING AUTHORS

Araceli G. Campaña: araceligc@ugr.es

Carlos Sánchez-Sánchez: cssanchez@icmm.csic.es

ORCID

Federico Villalobos: 0000-0001-5858-3833

Jesús I. Mendieta-Moreno: 0000-0001-8530-3315

Sara P. Morcillo: 0000-0002-6492-8866

José Ignacio Martínez Ruiz: 0000-0002-2086-8603

Jorge Lobo-Checa: 0000-0003-2698-2543

Jose Angel Martin-Gago (0000-0003-2663-491X)

Pedro L. de Andres: 0000-0002-9012-2890

Juan M. Cuerva: 0000-0001-6896-9617

Araceli G. Campaña: 0000-0001-5483-5642

Carlos Sánchez-Sánchez: 0000-0001-8644-3766

AUTHOR CONTRIBUTIONS

F.V. and J.I.M.-M. contributed equally to this work. All authors have given approval to the final version of the manuscript.

NOTES

The authors declare no competing financial interest.

ACKNOWLEDGMENT

We acknowledge financial support from Spanish MICIN/AEI/10.13039/501100011033 (PID2020-113142RB-C21, PID2022-138750NB-C21), and by MCIN/AEI/10.13039/501100011033 and the "European Union NextGenerationEU/PRTR" (PLEC2021-007906 and TED2021-129999B-C31), by the Comunidad de Madrid via Programa de Investigación Tecnologías 2018 (FOTOART-CM S2018/NMT-4367) and Programa Ayudas realización proyectos sinérgicos (FOTOSURF-CM, Y2020/NMT-6469), by the regional Governments of Aragon (E12_23R). F.V acknowledges financial support from Ministerio de Universidades (FPU18/05938). We further acknowledge the use of Servicio General de Apoyo a la Investigación-SAI and the Laboratorio de Microscopías Avanzadas of the Universidad de Zaragoza.

REFERENCES

(1) Gal, J. The Discovery of Biological Enantioselectivity: Louis Pasteur and the Fermentation of Tartaric Acid, 1857—A Review and Analysis 150 Yr Later. *Chirality* **2008**, *20* (1), 5–19. https://doi.org/10.1002/chir.20494.

(2) D'Angelo, J.; Smith, M. B. Chapter 6 - Stereochemistry. In *Hybrid Retrosynthesis*; D'Angelo, J., Smith, M. B., Eds.; Elsevier: Boston, 2015; pp 63–66. https://doi.org/10.1016/B978-0-12-411498-2.00006-1.

(3) Rieger, R.; Müllen, K. Forever Young: Polycyclic Aromatic Hydrocarbons as Model Cases for Structural and Optical Studies. *J of Physical Organic Chem* **2010**, *23* (4), 315–325. https://doi.org/10.1002/poc.1644.

(4) Chen, L.; Hernandez, Y.; Feng, X.; Müllen, K. From Nanographene and Graphene Nanoribbons to Graphene Sheets: Chemical Synthesis. *Angew Chem Int Ed* **2012**, *51* (31), 7640–7654. https://doi.org/10.1002/anie.201201084.

(5) Talirz, L.; Ruffieux, P.; Fasel, R. On-Surface Synthesis of Atomically Precise Graphene Nanoribbons. *Advanced Materials* **2016**, *28* (29), 6222–6231. https://doi.org/10.1002/adma.201505738.

(6) Pascal, R. A. Twisted Acenes. *Chem. Rev.* **2006**, *106* (12), 4809–4819. https://doi.org/10.1021/cr050550l.

(7) Gingras, M. One Hundred Years of Helicene Chemistry. Part 1: Non-Stereoselective Syntheses of Carbohelicenes. *Chem. Soc. Rev.* **2013**, *42* (3), 968–1006. https://doi.org/10.1039/C2CS35154D.

(8) Gingras, M.; Félix, G.; Peresutti, R. One Hundred Years of Helicene Chemistry. Part 2: Stereoselective Syntheses and Chiral Separations of Carbohelicenes. *Chem. Soc. Rev.* **2013**, *42* (3), 1007–1050. https://doi.org/10.1039/C2CS35111K.

(9) Gingras, M. One Hundred Years of Helicene Chemistry. Part 3: Applications and Properties of Carbohelicenes. *Chem. Soc. Rev.* **2013**, *42* (3), 1051–1095. https://doi.org/10.1039/C2CS35134J.

(10) Pun, S. H.; Miao, Q. Toward Negatively Curved Carbons. *Acc. Chem. Res.* **2018**, *51* (7), 1630–1642. https://doi.org/10.1021/acs.accounts.8b00140.

(11) Márquez, I. R.; Castro-Fernández, S.; Millán, A.; Campaña, A. G. Synthesis of Distorted Nanographenes Containing Seven- and Eight-Membered Carbocycles. *Chem. Commun.* **2018**, *54* (50), 6705–6718. https://doi.org/10.1039/C8CC02325E.

(12) Terrones, H.; Lv, R.; Terrones, M.; Dresselhaus, M. S. The Role of Defects and Doping in 2D Graphene Sheets and 1D Nanoribbons. *Rep. Prog. Phys.* **2012**, *75* (6), 062501. https://doi.org/10.1088/0034-4885/75/6/062501.

(13) Castro-Fernández, S.; Cruz, C. M.; Mariz, I. F. A.; Márquez, I. R.; Jiménez, V. G.; Palomino-Ruiz, L.; Cuerva, J. M.; Maçôas, E.; Campaña, A. G. Two-photon Absorption Enhancement by the Inclusion of a Tropone Ring in Distorted Nanographene Ribbons. *Angew. Chem. Int. Ed.* **2020**, anie.202000105. https://doi.org/10.1002/anie.202000105.

(14) Rickhaus, M.; Mayor, M.; Juríček, M. Chirality in Curved Polyaromatic Systems. *Chem. Soc. Rev.* **2017**, *46* (6), 1643–1660. https://doi.org/10.1039/C6CS00623J.

(15) *Polyarenes II*; Siegel, J. S., Wu, Y.-T., Eds.; Topics in Current Chemistry; Springer International Publishing: Cham, 2014; Vol. 350. https://doi.org/10.1007/978-3-319-07302-6.

(16) Lohr, T. G.; Urgel, J. I.; Eimre, K.; Liu, J.; Di Giovannantonio, M.; Mishra, S.; Berger, R.; Ruffieux, P.; Pignedoli, C. A.; Fasel, R.; Feng, X. On-Surface Synthesis of Non-Benzenoid Nanographenes by Oxidative Ring-Closure and Ring-Rearrangement Reactions. *J. Am. Chem. Soc.* **2020**, *142* (31), 13565–13572. https://doi.org/10.1021/jacs.0c05668.

(17) Fujii, S.; Marqués-González, S.; Shin, J.-Y.; Shinokubo, H.; Masuda, T.; Nishino, T.; Arasu, N. P.; Vázquez, H.; Kiguchi, M. Highly-Conducting Molecular Circuits Based on Antiaromaticity. *Nat Commun* **2017**, *8* (1), 15984. https://doi.org/10.1038/ncomms15984.

(18) Paquette, L. A. The Renaissance in Cyclooctatetraene Chemistry. *Tetrahedron* **1975**, *31* (23), 2855–2883. https://doi.org/10.1016/0040-4020(75)80303-6.

(19) Bachrach, S. M. Tetraphenylene Ring Flip Revisited. *J. Org. Chem.* **2009**, *74* (9), 3609–3611. https://doi.org/10.1021/jo900413d.

(20) Anet, F. A. L.; Bourn, A. J. R.; Lin, Y. S. Ring Inversion and Bond Shift in Cyclooctatetraene Derivatives. *J. Am. Chem. Soc.* **1964**, *86* (17), 3576–3577. https://doi.org/10.1021/ja01071a046.

(21) Huang, H.; Stewart, T.; Gutmann, M.; Ohhara, T.; Niimura, N.; Li, Y.-X.; Wen, J.-F.; Bau, R.; Wong, H. N. C. To Flip or Not To Flip? Assessing the Inversion Barrier of the Tetraphenylene Framework with Enantiopure 2,15-Dideuteriotetraphenylene and 2,7-Dimethyltetraphenylene. *J. Org. Chem.* **2009**, *74* (1), 359–369. https://doi.org/10.1021/jo802061p.

(22) Kroeger, A. A.; Karton, A. π–π Catalysis in Carbon Flatland—Flipping [8]Annulene on Graphene. *Chemistry A European J* **2021**, *27* (10), 3420–3426. https://doi.org/10.1002/chem.202004045.

(23) Kroeger, A. A.; Karton, A. Graphene-Induced Planarization of Cyclooctatetraene Derivatives. *Journal of Computational Chemistry* **2022**, *43* (2), 96–105. https://doi.org/10.1002/jcc.26774.

(24) González Miera, G.; Matsubara, S.; Kono, H.; Murakami, K.; Itami, K. Synthesis of Octagon-Containing Molecular Nanocarbons. *Chem. Sci.* **2022**, *13* (7), 1848–1868. https://doi.org/10.1039/D1SC05586K.

(25) Medel, M. A.; Tapia, R.; Blanco, V.; Miguel, D.; Morcillo, S. P.; Campaña, A. G. Octagon-Embedded Carbohelicene as a Chiral Motif for Circularly Polarized Luminescence Emission of Saddle-Helix Nanographenes. *Angew Chem Int Ed* **2021**, *60* (11), 6094–6100. https://doi.org/10.1002/anie.202015368.

(26) Clair, S.; De Oteyza, D. G. Controlling a Chemical Coupling Reaction on a Surface: Tools and Strategies for On-Surface Synthesis. *Chem. Rev.* **2019**, *119* (7), 4717–4776. https://doi.org/10.1021/acs.chemrev.8b00601.

(27) Hapala, P.; Kichin, G.; Wagner, C.; Tautz, F. S.; Temirov, R.; Jelínek, P. Mechanism of High-Resolution STM/AFM Imaging with Functionalized Tips. *Phys. Rev. B* **2014**, *90* (8), 085421. https://doi.org/10.1103/PhysRevB.90.085421.

(28) Gross, L.; Schuler, B.; Pavlicˇek, N.; Fatayer, S.; Majzik, Z.; Moll, N.; PeÇa, D.; Meyer, G. Atomic Force Microscopy for Molecular Structure Elucidation. *Angew. Chem. Int. Ed.* **2018**.

(29) Wang, J.; Niu, K.; Xu, C.; Zhu, H.; Ding, H.; Han, D.; Zheng, Y.; Xi, J.; You, S.; Deng, C.; Lin, H.; Rosen, J.; Zhu, J.; Björk, J.; Li, Q.; Chi, L. Influence of Molecular Configurations on the Desulfonylation Reactions on Metal Surfaces. *J. Am. Chem. Soc.* **2022**, *144* (47), 21596–21605. https://doi.org/10.1021/jacs.2c08736.

(30) Voigt, J.; Martin, K.; Neziri, E.; Baljozović, M.; Wäckerlin, C.; Avarvari, N.; Ernst, K. Highly Stereospecific On-Surface Dimerization into Bishelicenes: Topochemical Ullmann Coupling of

Bromohelicene on Au(111). *Chemistry A European J* **2023**, *29* (28), e202300134. https://doi.org/10.1002/chem.202300134.

(31) Mairena, A.; Wäckerlin, C.; Wienke, M.; Grenader, K.; Terfort, A.; Ernst, K.-H. Diastereoselective Ullmann Coupling to Bishelicenes by Surface Topochemistry. *J. Am. Chem. Soc.* **2018**, *140* (45), 15186–15189. https://doi.org/10.1021/jacs.8b10059.

(32) Irziqat, B.; Cebrat, A.; Baljozović, M.; Martin, K.; Parschau, M.; Avarvari, N.; Ernst, K.-H. Stereospecific On-Surface Cyclodehydrogenation of Bishelicenes: Preservation of Handedness from Helical to Planar Chirality. *Chemistry – A European Journal* **2021**, *27* (54), 13523–13526. https://doi.org/10.1002/chem.202102069.

(33) Stolz, S.; Bauer, M.; Pignedoli, C. A.; Krane, N.; Bommert, M.; Turco, E.; Bassi, N.; Kinikar, A.; Merino-Dìez, N.; Hany, R.; Brune, H.; Gröning, O.; Widmer, R. Asymmetric Azide-Alkyne Huisgen Cycloaddition on Chiral Metal Surfaces. *Commun Chem* **2021**, *4* (1), 1–7. https://doi.org/10.1038/s42004-021-00488-0.

(34) Stolz, S.; Danese, M.; Di Giovannantonio, M.; Urgel, J. I.; Sun, Q.; Kinikar, A.; Bommert, M.; Mishra, S.; Brune, H.; Gröning, O.; Passerone, D.; Widmer, R. Asymmetric Elimination Reaction on Chiral Metal Surfaces. *Advanced Materials* **2022**, *34* (2), 2104481. https://doi.org/10.1002/adma.202104481.

(35) Merino-Diez, N.; Amador, R.; Stolz, S. T.; Passerone, D.; Widmer, R.; Gröning, O. Asymmetric Molecular Adsorption and Regioselective Bond Cleavage on Chiral PdGa Crystals. *Advanced Science* **2024**, *11* (16), 2309081. https://doi.org/10.1002/advs.202309081.

(36) Stetsovych, O.; Švec, M.; Vacek, J.; Chocholoušová, J. V.; Jančařík, A.; Rybáček, J.; Kosmider, K.; Stará, I. G.; Jelínek, P.; Starý, I. From Helical to Planar Chirality by On-Surface Chemistry. *Nature Chem* **2017**, *9* (3), 213–218. https://doi.org/10.1038/nchem.2662.

(37) Mallada, B. On-Surface Strain-Driven Synthesis of Nonalternant Non-Benzenoid Aromatic Compounds Containing Four- to Eight-Membered Rings. *Journal of the American Chemical Society* 9.

(38) Cai, J.; Ruffieux, P.; Jaafar, R.; Bieri, M.; Braun, T.; Blankenburg, S.; Muoth, M.; Seitsonen, A. P.; Saleh, M.; Feng, X.; Müllen, K.; Fasel, R. Atomically Precise Bottom-up Fabrication of Graphene Nanoribbons. *Nature* **2010**, *466* (7305), 470–473. https://doi.org/10.1038/nature09211.

(39) Geagea, E.; Medina-Lopez, D.; Giovanelli, L.; Nony, L.; Loppacher, C.; Campidelli, S.; Clair, S. Growth Mechanism of Chevron Graphene Nanoribbons on (111)-Oriented Coinage Metal Surfaces. *J. Phys. Chem. C* **2024**, acs.jpcc.4c01080. https://doi.org/10.1021/acs.jpcc.4c01080.

(40) Márquez, I. R.; Ruíz Del Árbol, N.; Urgel, J. I.; Villalobos, F.; Fasel, R.; López, M. F.; Cuerva, J. M.; Martín-Gago, J. A.; Campaña, A. G.; Sánchez-Sánchez, C. On-Surface Thermal Stability of a Graphenic Structure Incorporating a Tropone Moiety. *Nanomaterials* **2022**, *12* (3), 488. https://doi.org/10.3390/nano12030488.

(41) Fan, Q.; Martin-Jimenez, D.; Ebeling, D.; Krug, C. K.; Brechmann, L.; Kohlmeyer, C.; Hilt, G.; Hieringer, W.; Schirmeisen, A.; Gottfried, J. M. Nanoribbons with Nonalternant Topology from Fusion of Polyazulene: Carbon Allotropes beyond Graphene. *J. Am. Chem. Soc.* **2019**, *141* (44), 17713–17720. https://doi.org/10.1021/jacs.9b08060.

(42) Liu, J.; Mishra, S.; Pignedoli, C. A.; Passerone, D.; Urgel, J. I.; Fabrizio, A.; Lohr, T. G.; Ma, J.; Komber, H.; Baumgarten, M.; Corminboeuf, C.; Berger, R.; Ruffieux, P.; Müllen, K.; Fasel, R.; Feng, X. Open-Shell Nonbenzenoid Nanographenes Containing Two Pairs of Pentagonal and Heptagonal Rings. *J. Am. Chem. Soc.* **2019**, *141* (30), 12011–12020. https://doi.org/10.1021/jacs.9b04718.

(43) Hieulle, J.; Carbonell-Sanromà, E.; Vilas-Varela, M.; Garcia-Lekue, A.; Guitián, E.; Peña, D.; Pascual, J. I. On-Surface Route for Producing Planar Nanographenes with Azulene Moieties. *Nano Lett.* **2018**, *18* (1), 418–423. https://doi.org/10.1021/acs.nanolett.7b04309.

(44) Biswas, K.; Yang, L.; Ma, J.; Sánchez-Grande, A.; Chen, Q.; Lauwaet, K.; Gallego, J. M.; Miranda, R.; Écija, D.; Jelínek, P.; Feng, X.; Urgel, J. I. Defect-Induced π-Magnetism into Non-Benzenoid Nanographenes. *Nanomaterials* **2022**, *12* (2), 224. https://doi.org/10.3390/nano12020224.

(45) Hou, I. C.-Y.; Sun, Q.; Eimre, K.; Di Giovannantonio, M.; Urgel, J. I.; Ruffieux, P.; Narita, A.; Fasel, R.; Müllen, K. On-Surface Synthesis of Unsaturated Carbon Nanostructures with Regularly Fused Pentagon–Heptagon Pairs. *J. Am. Chem. Soc.* **2020**, *142* (23), 10291–10296. https://doi.org/10.1021/jacs.0c03635.

(46) Hafner, K.; Meinhardt, K.; Richarz, W. Cyclopent[*Cd*]Azulene and 1,2-Dihydrodicyclopent-[*Cd,Ij*]Azulene. *Angew. Chem. Int. Ed. Engl.* **1974**, *13* (3), 204–205. https://doi.org/10.1002/anie.197402041.

(47) Toda, T.; Minabe, M.; Yoshida, M.; Tobita, K. Electrophilic Substitution Reactions of Benz[a]Indeno[1,2,3-Cd]Azulene. *J. Org. Chem.* **1990**, *55* (4), 1297–1300. https://doi.org/10.1021/jo00291a037.

(48) Liu, H.-C.; Ruan, K.; Ma, K.; Fei, J.; Lin, Y.-M.; Xia, H. Synthesis of Metalla-Dual-Azulenes with Fluoride Ion Recognition Properties. *Nat Commun* **2023**, *14* (1), 5583. https://doi.org/10.1038/s41467-023-41250-5.

(49) Wu, F.; Barragán, A.; Gallardo, A.; Yang, L.; Biswas, K.; Écija, D.; Mendieta-Moreno, J. I.; Urgel, J. I.; Ma, J.; Feng, X. Structural Expansion of Cyclohepta[Def]Fluorene towards Azulene-Embedded Non-Benzenoid Nanographenes. *Chemistry – A European Journal* **2023**, *29* (51), e202301739. https://doi.org/10.1002/chem.202301739.

(50) Mendieta-Moreno, J. I.; Walker, R. C.; Lewis, J. P.; Gómez-Puertas, P.; Mendieta, J.; Ortega, J. FIREBALL / AMBER : An Efficient Local-Orbital DFT QM/MM Method for Biomolecular Systems. *J. Chem. Theory Comput.* **2014**, *10* (5), 2185–2193. https://doi.org/10.1021/ct500033w.

(51) Mendieta-Moreno, J. I.; Mallada, B.; De La Torre, B.; Cadart, T.; Kotora, M.; Jelínek, P. Unusual Scaffold Rearrangement in Polyaromatic Hydrocarbons Driven by Concerted Action of Single Gold Atoms on a Gold Surface. *Angew Chem Int Ed* **2022**, *61* (50), e202208010. https://doi.org/10.1002/anie.202208010.

(52) Björk, J.; Sánchez-Sánchez, C.; Chen, Q.; Pignedoli, C. A.; Rosen, J.; Ruffieux, P.; Feng, X.; Narita, A.; Müllen, K.; Fasel, R. The Role of Metal Adatoms in a Surface-Assisted Cyclodehydrogenation Reaction on a Gold Surface. *Angew Chem Int Ed* **2022**, *61* (49), e202212354. https://doi.org/10.1002/anie.202212354.

(53) Liu, X.; Matej, A.; Kratky, T.; Mendieta-Moreno, J. I.; Günther, S.; Mutombo, P.; Decurtins, S.; Aschauer, U.; Repp, J.; Jelinek, P.; Liu, S.-X.; Patera, L. L. Exploiting Cooperative Catalysis for

the On-Surface Synthesis of Linear Heteroaromatic Polymers via Selective C–H Activation. *Angewandte Chemie International Edition* **2022**, *61* (5), e202112798. https://doi.org/10.1002/anie.202112798.

(54) McNamara, O. A.; Maguire, A. R. The Norcaradiene–Cycloheptatriene Equilibrium. *Tetrahedron* **2011**, *67* (1), 9–40. https://doi.org/10.1016/j.tet.2010.10.030.

(55) Bronner, C.; Durr, R. A.; Rizzo, D. J.; Lee, Y.-L.; Marangoni, T.; Kalayjian, A. M.; Rodriguez, H.; Zhao, W.; Louie, S. G.; Fischer, F. R.; Crommie, M. F. Hierarchical On-Surface Synthesis of Graphene Nanoribbon Heterojunctions. *ACS Nano* **2018**, *12* (3), 2193–2200. https://doi.org/10.1021/acsnano.7b08658.

(56) Teeter, J. D.; Zahl, P.; Mehdi Pour, M.; Costa, P. S.; Enders, A.; Sinitskii, A. On-Surface Synthesis and Spectroscopic Characterization of Laterally Extended Chevron Graphene Nanoribbons. *ChemPhysChem* **2019**, *20* (18), 2281–2285. https://doi.org/10.1002/cphc.201900445.

(57) Jacobse, P. H.; McCurdy, R. D.; Jiang, J.; Rizzo, D. J.; Veber, G.; Butler, P.; Zuzak, R.; Louie, S. G.; Fischer, F. R.; Crommie, M. F. Bottom-up Assembly of Nanoporous Graphene with Emergent Electronic States. *J. Am. Chem. Soc.* **2020**, *142* (31), 13507–13514. https://doi.org/10.1021/jacs.0c05235.

(58) Shekhirev, M.; Zahl, P.; Sinitskii, A. Phenyl Functionalization of Atomically Precise Graphene Nanoribbons for Engineering Inter-Ribbon Interactions and Graphene Nanopores. *ACS Nano* **2018**, *12* (8), 8662–8669. https://doi.org/10.1021/acsnano.8b04489.